Science in China Series E: Technological Sciences

www.scichina.com
tech.scichina.com
www.springerlink.com

3-dimensional slope stability analyses using non-associative stress-strain relationships

CHEN ZuYu[1†], SUN Ping[1], WANG YuJie[1] & ZHANG HongTao[2]

[1] Department of Geotechnical Engineering, China Institute of Water Resources and Hydropower Research, Beijing 100048, China;
[2] Department of Civil Engineering, Beijing University of Science and Technology, Beijing 430074, China

The research work presented in this paper refers to a new slope stability analysis method used for landslide risk evaluations. It is an extension of the 3-dimensional upper-bound slope stability analysis method proposed by Chen et al. in 2001, which employs the Mohr-Coulomb's associative flow rule. It has been found that in a 3-dimensional area, a prism may not be able to move at friction angles to all its surrounding interfaces, as required by this associative rule, and convergence problems may occasionally arise. The new method establishes two velocity fields: (i) The plastic one that represents a non-associative and the best representative dilation behavior, and (ii) the virtual one that permits the solution for factor of safety in the work and energy balance equation. The new method can then allow any input value of dilation angle and thus solve the convergence problem. A practical application to a concrete dam foundation is illustrated.

non-associative flow rule, slope stability, limit analysis, 3-dimension

1 Introduction

Most slope failures have distinct 3-dimensional features. Extending the currently used 2-dimensional limit equilibrium and limit analysis methods to the area of 3-dimensions has drawn wide attentions.

The limitations of the limit equilibrium methods, as discussed by Chen et al.[1], stimulated the efforts of developing a more rigorous method based on the upper-bound theory of plasticity. In the 2D area, Chen and Donald[2] developed a numerical method that divides the failure mass into a number of slices with inclined interfaces where shear failure prevails. The method started from establishing a compatible velocity field in which each slice dilates with the friction angles to the base and interfaces, as suggested by the Mohr-Coulomb's associative flow rule. The factor of safety was obtained by the work and energy balance equation. The optimization method would find the critical location of the slip surface and inclinations of the interfaces associated with the minimum factor of safety. This method has succeeded in obtaining the results for a series of testing problems, which are identical to the theoretical solutions provided by Sokolovski[3] both in terms of the minimum factor of safety and the critical failure modes.

Extensions of the 2D upper-bound method to 3-dimensions were reported by Michalowski[4], and later updated by Farzaneh and Askari[5]. Their methods involve only a few numbers of blocks and their applications are limited to slopes with symmetric and homogeneous geometric and material behavior. Chen et al.[6, 7] developed a new method that divides the failure mass into a series of columns to release the limitations. It is actually a 3D extension of the 2D approaches by Donald and Chen[2].

However, using the associative flow rule necessitates a dilatation direction to be equal to the friction angle ϕ of the sliding mass and has consequently caused con-

Received April 1, 2009; accepted June 6, 2009
doi: 10.1007/s11431-009-0276-0
†Corresponding author (email: chenzuyu@iwhr.com)
Supported by the National Natural Science Foundation (Grant Nos. 50539100, 50509027)

Citation: Chen Z Y, Sun P, Wang Y J, et al. 3-dimensional slope stability analyses using non-associative stress-strain relationships. Sci China Ser E-Tech Sci, 2009, 52(9): 2517−2527, doi: 10.1007/s11431-009-0276-0

vergence problems in some 3D numerical calculations, especially in rock masses where the value of ϕ can be quite big. On the other hand, the large dilatation angles assigned on the shear surfaces can be physically unrealistic.

This paper is aimed at updating this 3D upper-bound slope stability method by introducing non-associative stress-strain relationships. In the new method, the prism would develop a plastic velocity that dilates at any arbitrary angle ψ, while the normal and shear stresses on the failure surface still obey Mohr-Coulomb's failure criterion associated with true friction angle ϕ.

2 Discussions on some background understandings

2.1 The plastic and virtual velocities

In the upper bound analysis, the Mohr-Coulomb's associative flow rule is normally used to define the plastic velocity developed by an increment of external load, which inclines at a friction angle, ϕ, to the failure surface, as illustrated by the following equation (see Figure 1(a))

$$\frac{V_n}{V_s} = \frac{\partial f / \partial t}{\partial f / \partial \tau} = -\tan\phi, \tag{1}$$

where V_n and V_s are normal and tangential velocities, respectively, τ and σ are effective tangential and normal stresses, respectively. They obey the following relationship

$$f(\tau,\sigma) = \tau - c - (\sigma - u)\tan\phi = 0, \tag{2}$$

where u is the pore pressure applied on the failure surface.

The work done by the internal total stress of the failure surface can be determined as

$$\begin{aligned} D &= (\tau V_s - \sigma V_n)A = (\tau\cos\phi - \sigma\sin\phi)VA \\ &= (c\cos\phi - u\sin\phi)VA, \end{aligned} \tag{3}$$

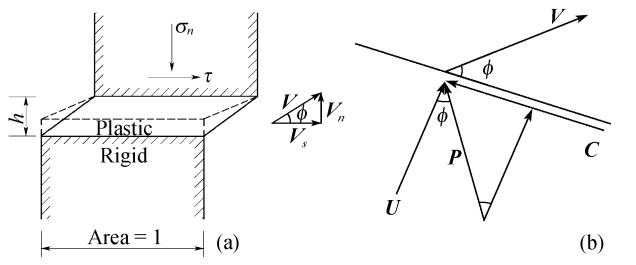

Figure 1 The Mohr-Coulomb's associative flow rule and energy dissipation. (a) Normal and tangential velocities; (b) The 'combined friction force' ***P***.

where A is the area of the failure surface and V the magnitude of the velocity.

The advantage of adopting Mohr-Coulomb's associative flow rule is that the energy dissipation can be determined without the knowledge of the internal stresses, which are generally unknown.

Eq. (3) can be illustrated by Figure 1(b) in which the internal forces applied on the failure surface consist of three parts: 1) the shear force contributed by cohesion, which is known as cA, denoted as ***C*** in Figure 1(b); 2) the resultant of the normal effective force ***N*** and the shear resistance contributed by the friction, denoted as ***P***, that inclines at an angle of ϕ and is called 'combined friction force' by Chen[8]; 3) the pore pressure with a magnitude of uA, denoted as ***U***.

Now assuming that the failure mass moves with a velocity ***V*** that inclines at an angle of ϕ to the failure surface and allowing all the internal forces to do work on ***V***, we can find that ***VP*** is zero as ***V*** is perpendicular to ***P***, leaving only ***C*** and ***U*** that make eq. (3) stand.

In a 3-dimensional system consisting of n prisms shown in Figure 2, given the conventional definition of factor of safety F, which reduces the available shear strength parameters by the following equations

$$c_e = c / F, \tag{4}$$

$$\tan\phi_e = \tan\phi / F, \tag{5}$$

the work-energy balance equation for the whole system is

$$\sum D^*_{i\leftrightarrow j,e} + \sum D^*_{i\updownarrow j,e} + \sum D^*_{i,j,e} = WV^* + T^0V^*. \tag{6}$$

The three terms on the left-hand side of eq. (6) refer to the energy dissipations on the 'row-to-row', 'column-to-column' interfaces, designated by $\leftrightarrow$ and $\updownarrow$ in Figure 3, and on the slip surface, respectively. The subscript 'e' means that D is determined by eq. (3) on the basis of the reduced strength parameters defined by eqs. (4) and (5).

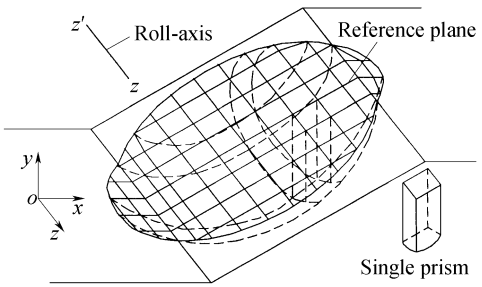

Figure 2 An isometric view of the discretization pattern for a 3-dimensional failure mass.

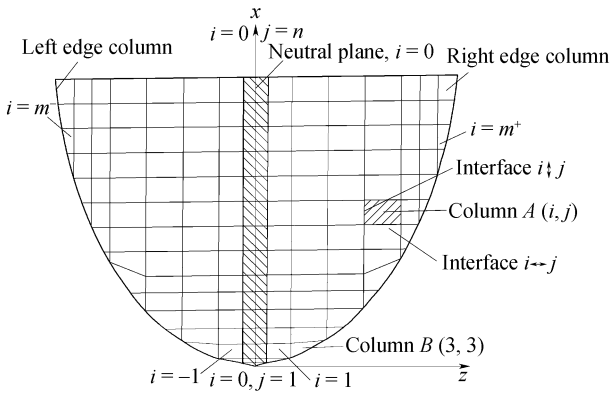

Figure 3 A plan view of the discretization pattern for a 3-dimensional failure.

For the remainder of this paper, the subscript '*e*' is attached to any variable that has been calculated using these reduced strength parameters, meaning an unknown coefficient F is involved there. $\boldsymbol{V}^*$ is a postulated plastic velocity field for a given failure mechanism, which is separately determined based on the flow rule and the requirement for displacement compatibility. Once $\boldsymbol{V}^*$ is determined, eq. (6) has only one unknown, the factor of safety, which is implicitly involved in the subscript '*e*'. The computation procedure for a 3D failure pattern is thus considerably facilitated. An optimization procedure will be followed to find the minimum factor of safety among all possible $\boldsymbol{V}^*$ associated with different failure patterns that include the locations of slip surfaces and inclinations of the interfaces.

The velocity field $\boldsymbol{V}$ can then be comprehended by the following understandings.

1) $\boldsymbol{V}$ is a plastic velocity field that makes the manipulation, based on eq. (6), supported by the upper-bound theory of plasticity.

2) $\boldsymbol{V}$ can be regarded as a virtual velocity field involved in a manipulation similar to the virtual work principle based on eq. (6). Its unique feature of having a direction inclined at ϕ_e to the failure surface allows the elimination of all the unknown internal forces and consequently renders the formulation numerically tractable using eq. (3).

In the traditional upper method, the plastic and virtual velocities are identical. The method thus enjoys both advantages of theoretical rigorousness and numerical tractability. However, as discussed in the introduction, fixing a specified dilatation angle, which is ϕ, may be either physically unrealistic or practically impossible if the friction angle is too big. Here, the question arises of the possibility of assigning a velocity that dilates at any angle to the failure surface. The direct impact of having a velocity that does not dilate at a friction angle ϕ is that in Figure 1(b), $\boldsymbol{V}$ would not be perpendicular to $\boldsymbol{P}$ and $\boldsymbol{VP}$ would no longer be zero. To solve this problem, a concept of separating the plastic and virtual velocities into a 'bi-velocity' field is developed, as will be discussed in the subsequent section.

2.2 The 'bi-velocity field'

In the formulation for determining the internal energy dissipation shown in eq.(3), an assumption was implied that the normal force $\boldsymbol{N}$, shear force $\boldsymbol{C}$ contributed by cohesion, the 'combined friction force' $\boldsymbol{P}$, and the plastic velocity $\boldsymbol{V}$ lie on the same plane, designated by Λ (Figure 4). This assumption forms the basis for all upper-bound methods in plasticity as it is this postulate that enables eq. (3) to stand, as discussed by Chen[9].

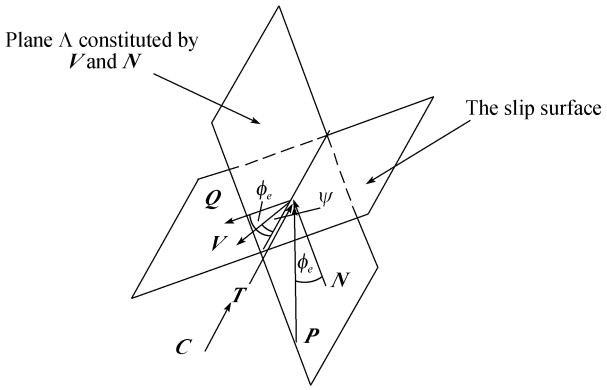

Figure 4 The plane Λ on which $\boldsymbol{N}$, $\boldsymbol{C}$, $\boldsymbol{P}$, $\boldsymbol{V}$ and $\boldsymbol{Q}$ lie.

By introducing the postulate of 'coincidence of principle stress and strain axes', it is possible to determine the direction of the shear stress applied on the failure surface based on that of the plastic velocity. By intersecting plane Λ constituted by $\boldsymbol{N}$ and $\boldsymbol{V}$ with the failure surface, the directions of $\boldsymbol{C}$ and $\boldsymbol{P}$ can be fully identified (see Figure 4). The number of unknowns involved in the force equilibrium equations of each prism is thus reduced. The manipulation based on the equation of virtual work, similar to eq. (6), can be performed in the 3D limit analysis method by introducing a virtual velocity $\boldsymbol{Q}^*$ on plane Λ. $\boldsymbol{Q}^*$ inclines at an angle of ϕ_e to the failure plane and enables the following equation to stand:

$$\sum \boldsymbol{D}^*_{i\leftrightarrow j} + \sum \boldsymbol{D}^*_{i\updownarrow j} + \sum \boldsymbol{D}^*_{i,j} = \boldsymbol{W}\boldsymbol{Q}^* + \boldsymbol{T}^0\boldsymbol{Q}^*, \qquad (7)$$

$\boldsymbol{V}$ and $\boldsymbol{Q}$ form a 'bi-velocity field' that permits the following procedure for a limit analysis method employing

non-associative stress-strain relationships.

1) For a prism, determine a velocity $\boldsymbol{V}$ that dilates at ψ, an angle specified by the user to represent a non-associative relationship of $\boldsymbol{V}_n$ and $\boldsymbol{V}_s$ as follows

$$\frac{V_n}{V_s} = \frac{\partial f / \partial \sigma}{\partial f / \partial \tau} = -\tan\psi, \tag{8}$$

where f is a yield function on a non-associative flow rule that is not necessarily represented by eq. (2).

2) Once the velocity field $\boldsymbol{V}$ is obtained, the plane Λ for each prism can be constituted by $\boldsymbol{V}$ and $\boldsymbol{N}$. On this plane, establish a virtual velocity $\boldsymbol{Q}$ that inclines at ϕ_e to the failure surface, i.e., a vector perpendicular to the 'combine frictional force $\boldsymbol{P}'$.

3) Establish the virtual work equation according to eq. (7) and solve for the factor of safety.

2.3 Stability analysis for wedge failure analyses——An example using the 'bi-velocity field'

As a pilot work, the first author of this paper successfully investigated the feasibility of using this bi-velocity concept on the analysis of the simplest 3-dimensional case——A tetrahedral rock wedge.

It has been found that the limit equilibrium method commonly used for a tetrahedral rock wedge stability analysis is statically indeterminate. Different inputs of the directions of shear forces on the left and right planes will give different solutions of factor of safety. The conventional method[10] neglects the shear force components when formulating the equations for determining the normal forces on a cross section perpendicular to the line of intersection, as illustrated in Figure 5. This actually assumes that the shear forces applied on the failure planes are parallel to the line of intersection and the wedge dilates at a zero angle to the failure planes. Perhaps Pan[10] was the first who argued this assumption and put forward his "postulates of maximum and minimum'. Initiated from this postulate, a new method that allows any arbitrary shear force directions on the failure planes was developed and documented by Chen[8].

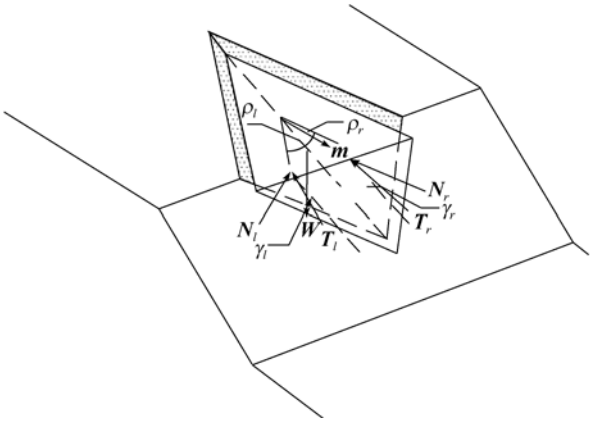

Figure 5 The generalized method for wedge stability analysis.

This method starts from establishing a plastic wedge velocity $\boldsymbol{m}$, representing a pair of dilation angles ρ_l and ρ_r to the left and right failure planes, respectively (Figure 5).

The generalized solutions to factor of safety can be obtained by the following procedure.

1) Given $\boldsymbol{m}$, the directions of shear force vectors $\boldsymbol{T}$ on the left and right failure planes can be determined by intercepting plane Λ with the slip surface as illustrated in Figure 4.

2) Once $\boldsymbol{T}_l$ and $\boldsymbol{T}_r$ are determined, the directions of the 'combined frictional forces' $\boldsymbol{P}_l$ and $\boldsymbol{P}_r$, applied on the two failure planes are known. By projecting all the forces applied on the wedge to an axis that is perpendicular to $\boldsymbol{P}_l$ and $\boldsymbol{P}_r$, designated by $\boldsymbol{Q}$, it is possible to obtain an equation that only involves the unknown factor of safety, i.e.,

$$\boldsymbol{Q}\cdot\boldsymbol{C}_{el} + \boldsymbol{Q}\cdot\boldsymbol{C}_{er} + \boldsymbol{Q}\cdot\boldsymbol{W} = 0, \tag{9}$$

which leads to a generalized solution to the wedge stability problems.

$$\begin{aligned}\Omega(\rho_l,\rho_r,F) = &-\cos\phi_{el}\cos(\rho_r-\phi_{er})c_{el}A_l\\ &-\cos\phi_{er}\cos(\rho_l-\phi_{el})c_{er}A_r\\ &+[\sin\phi_{el}\cos(\rho_r-\phi_{er})b_w\\ &+\cos(\rho_l-\phi_{el})\sin\phi_{er}c_w\\ &+a_w\cos(\rho_l-\phi_{el})\cos(\rho_r-\phi_{er})]W\\ &=0,\end{aligned} \tag{10}$$

where a_w, b_w, and c_w are coefficients calculated based on the information of $\boldsymbol{W}$ (refer to Chen[8] for details).The factor of safety can then be solved through iterations. Chen[8] further demonstrated that a maximum factor of safety exists when the wedge dilates at friction angles to the failure planes, i.e., if $\rho_l = \phi_{el}$ and $\rho_r = \phi_{er}$, then we have $\dfrac{\partial F}{\partial \rho_l} = 0$ and $\dfrac{\partial F}{\partial \rho_r} = 0$.

3 The generalized method

3.1 The methodology

With the background knowledge described in Section 2, we can now establish a generalized method applicable to a problem involving a multi-wedge system:

1) Create a virtual velocity $\boldsymbol{Q}$ that is perpendicular to $\boldsymbol{P}_l$ and $\boldsymbol{P}_r$ for each prism;

2) Establish the work-energy balance equation based on this virtual velocity, which is exactly eq. (9), but in a summation form for a system consisting of multi-wedges.

$$\sum(\boldsymbol{Q}\cdot\boldsymbol{C}_{el}+\boldsymbol{Q}\cdot\boldsymbol{C}_{er}+\boldsymbol{Q}\cdot\boldsymbol{W})=0. \tag{11}$$

The computation procedure of the generalized method takes a way similar to that of the method using associative flow rule proposed by Chen et al.[1].

An assumption is made that inside the failure mass there exists a plane, called the 'neutral plane', on which there is no lateral movement relative to the main direction of sliding. This plane serves as the *ox*-*oy* coordinate system, while *oz* is perpendicular to it in a clock-wise direction (Figure 2).

The failure mass is divided into a series of prisms as shown in Figure 2, whose plan view is shown in Figure 3. Each prism is approximated by a hexahedron. The 'row-to-row' interfaces are front and rear surfaces, respectively, and are represented by the symbol $\leftrightarrow$. They are perpendicular to the plane *xoy*. The 'column to column' interfaces are perpendicular to the plane *xoz*, and represented by the symbol $\updownarrow$.

The idea of 'neutral plane' is now extended to be a 'reference plane', on which the prism moves at dilation angles ψ_l and ψ_r to its left and right bases as shown in Figure 6.

3.2 Calculating the plastic velocity field that obeys the non-associative relationship

From now on, the dilation angle ψ is reduced to ψ_e in a similar way to eq. (5).

$$\tan\psi_e=\tan\psi/F. \tag{12}$$

This treatment means that the dilation and friction angles have a same safety margin. The plastic velocity of a prism relative to its immediate neighbors is calculated on the basis of satisfying the non-associative relationship and displacement compatibility. It consists of two procedures (for detailed formulation, please refer to [6, 11]).

1) Calculating the plastic velocity field $\boldsymbol{V}$ of the prisms at the reference plane.

As discussed previously, the velocities of prisms at the reference plane are determined independently of their neighboring prisms. Each prism on this plane is then regarded as a wedge as discussed in Section 2.3 and shown in Figure 6. The unit vector of velocity $\boldsymbol{V}_{0,j}$, denoted as $\boldsymbol{m}_{0,j}$, can be determined by simple vector analysis. The magnitude of $\boldsymbol{V}_{0,j}$ is determined by the condition of displacement compatibility, which requires that $\boldsymbol{V}_{0,j}$ determined by eq. (13) be inclined at $\psi_{e,0,j}$ to the row-to-row interface numbered $\psi_{0,j}$.

$$\boldsymbol{V}_{0\leftrightarrow j}=\boldsymbol{V}_{0,j}-\boldsymbol{V}_{0,j-1}. \tag{13}$$

2) Calculating the plastic velocity field $\boldsymbol{V}$ of the prisms other than those on the reference plane

The velocity $\boldsymbol{V}_{i,j}$ of prism i, j is determined based on the velocities of their left and lower neighbouring prisms $\boldsymbol{V}_{i\text{-}1,j}$ and $\boldsymbol{V}_{i,j\text{-}1}$.

$$\begin{aligned}&\Phi(\boldsymbol{V}_{i,j},\boldsymbol{N}_{i,j})=\sin\psi_{e,i,j},\\&\Phi(\boldsymbol{V}_{i\updownarrow j},\boldsymbol{N}_{i\updownarrow j})=\sin\psi_{e,i\updownarrow j},\\&\Phi(\boldsymbol{V}_{i\leftrightarrow j},\boldsymbol{N}_{i\leftrightarrow j})=\sin\psi_{e,i\leftrightarrow j},\end{aligned} \tag{14}$$

where $\Phi(\boldsymbol{V}, \boldsymbol{N})$ represents cosine of the angle between the vectors $\boldsymbol{V}$ and $\boldsymbol{N}$ and can be determined by

$$\Phi(\boldsymbol{V},\boldsymbol{N})=\frac{X\cdot L+Y\cdot M+Z\cdot N}{\sqrt{X^2+Y^2+Z^2}\cdot\sqrt{L^2+M^2+N^2}}, \tag{15}$$

where X, Y, Z are components of $\boldsymbol{V}$, and L, M, N the direction cosines of the normal to the failure plane.

Since $\boldsymbol{V}_{i-1,j}$ and $\boldsymbol{V}_{i,j-1}$ are known, eqs. (14) are suffi

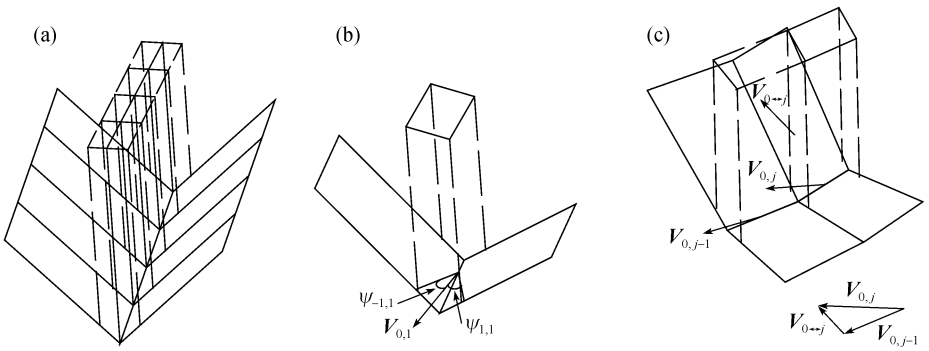

Figure 6 Determining velocities of the prisms on the reference plane. (a) Sketch of the prisms, (b) the velocity of the first prism, (c) the velocities of two contiguous prisms.

cient to determine the three components of $\boldsymbol{V}_{i,j}$ with the definitions

$$\boldsymbol{V}_{i\leftrightarrow j}=\boldsymbol{V}_{i,j}-\boldsymbol{V}_{i,j-1}, \tag{16}$$

$$\boldsymbol{V}_{i\updownarrow j}=\boldsymbol{V}_{i,j}-\boldsymbol{V}_{i-1,j}. \tag{17}$$

3.3 Calculating the virtual velocities that are perpendicular to the 'combined frictional forces'

The next step is to determine the virtual velocity field $\boldsymbol{Q}$, which in turn comprises the following procedures.

1) Calculating the direction of the combined frictional force $\boldsymbol{P}$ (Chen et al.[12]).

Given the direction of the plastic velocity of a prism $\boldsymbol{V}$, it is possible to determine the direction of the combined frictional force $\boldsymbol{P}$ that lies on plane Λ, constituted by normal force $\boldsymbol{N}$ and $\boldsymbol{V}$ (Figure 4). By denoting the unit vectors of $\boldsymbol{N}$ and $\boldsymbol{V}$ by $\boldsymbol{n}$ and $\boldsymbol{m}$, respectively, $\boldsymbol{P}$ is given by the following relationship (Figure 7)

$$\boldsymbol{P}=|\boldsymbol{a}|\cdot\boldsymbol{n}-|\boldsymbol{b}|\cdot\boldsymbol{m}. \tag{18}$$

From the vector triangle shown in Figure 7, it is easy to find that

$$\frac{|\boldsymbol{a}|}{\sin\left(\frac{\pi}{2}+\psi_e-\phi_e\right)}=\frac{|\boldsymbol{b}|}{\sin\phi_e}=\frac{|\boldsymbol{c}|}{\sin\left(\frac{\pi}{2}-\psi_e\right)}. \tag{19}$$

Since only the direction of $\boldsymbol{P}$ is concerned, $|\boldsymbol{c}|$ may be taken as unity, and we have

$$|\boldsymbol{a}|=\frac{\sin\left(\frac{\pi}{2}+\psi_e-\phi_e\right)}{\sin\left(\frac{\pi}{2}-\psi_e\right)}=\frac{\cos(\psi_e-\phi_e)}{\cos\psi_e}, \tag{20}$$

$$|\boldsymbol{b}|=\frac{\sin\phi_e}{\sin\left(\frac{\pi}{2}-\psi_e\right)}=\frac{\sin\phi_e}{\cos\psi_e}. \tag{21}$$

Substituting eqs. (20), (21) into (18), we have

$$\boldsymbol{P}=\frac{\cos(\psi_e-\phi_e)}{\cos\psi_e}\boldsymbol{n}-\frac{\sin\phi_e}{\cos\psi_e}\boldsymbol{m}. \tag{22}$$

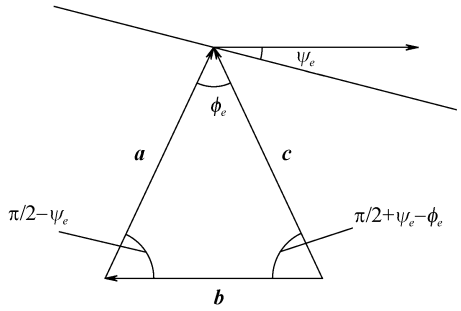

Figure 7 The triangle defining the 'combined frictional force' $\boldsymbol{P}$.

By denoting the unit vector of $\boldsymbol{P}$ by $\boldsymbol{p}$, for a given prism numbered i, j, $\boldsymbol{p}_{i,j}, \boldsymbol{p}_{i\updownarrow j}, \boldsymbol{p}_{i\leftrightarrow j}$ can be respectively determined based on eq. (22).

2) Calculating the virtual velocity $\boldsymbol{Q}$ that is perpendicular to $\boldsymbol{P}$.

The virtual velocity $\boldsymbol{Q}$ can be determined by the relationships

$$\boldsymbol{Q}_{i,j}\cdot\boldsymbol{p}_{i,j}=0,\ \boldsymbol{Q}_{i\updownarrow j}\cdot\boldsymbol{p}_{i\updownarrow j}=0,\ \boldsymbol{Q}_{i\leftrightarrow j}\cdot\boldsymbol{p}_{i\leftrightarrow j}=0. \tag{23}$$

3) Calculating the factor of safety by the equation of virtual work.

Once the virtual velocity field is determined, the factor of safety can be calculated by eq. (7) through iterations.

4 Test examples and practical applications

4.1 Zhang's example with ellipsoidal spherical slip surfaces

The example depicted by Zhang[13] has been widely used in literature for validation purposes (Lam and Fredlund[14]; Huang and Tsai[15], Chen and Chameau[16], Chen et al.[17]). Figure 8 shows the geometry and geotechnical parameters of the problem. Chen et al.[17] summarized the calculated results for two cases obtained by different authors using the limit equilibrium and upper bound methods, which are reevaluated with the method described in this paper.

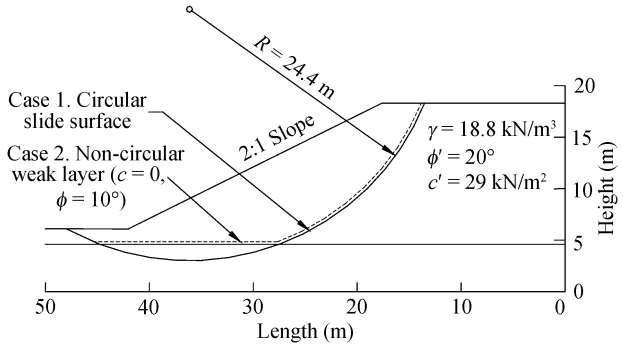

Figure 8 Zhang's Example 1 with an ellipsoidal spherical slip surface.

Case 1. The ellipsoidal spherical slip surface.

The slip surface has a circular shape at the central *xoy* plane and extends in the lateral *z* direction by elliptic lines. Figure 9 shows an isometric view of the failure mass divided by prisms with vertical interfaces. In the previous studies, Zhang gave a solution of F=2.122[13].

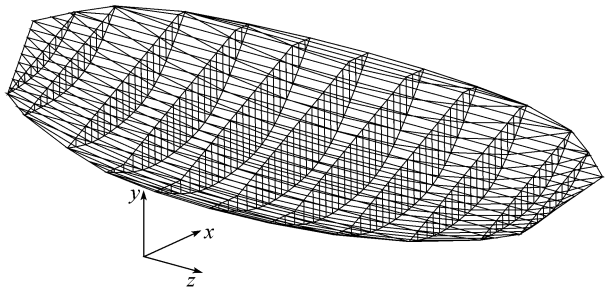

Figure 9 Case 1 of Zhang's Example 1, an isometric view of the failure mass with vertical interfaces.

The utilization of the 3D limit equilibrium method proposed by Chen et al.[17] found F=2.187.

Chen et al.[7] investigated the case using the upper-bound approaches, i.e., $\phi = \psi = 20°$. They obtained a factor of safety of F=2.262. For this particular problem, no convergence problem was encountered.

Analyses using different dilation angles of ψ have been carried out. An initial estimated failure mode using vertical inter-prism faces was first evaluated, with the similar diagram shown in Figure 9, followed by an optimization process that found the critical mode of interface inclinations associated with the minimum factor of safety.

Table 1 gives the factors of safety associated with different dilation angles ψ.

Table 1 Factors of safety associated with different dilation angles of ψ, Case 1 of Zhang's Example 1

ψ(°)	0	5	10	15	20
ψ_e (°)	0	2.28	4.54	6.81	9.09
F	2.176	2.196	2.219	2.246	2.262

Case 2. The ellipsoidal spherical slip surface with a weak seam.

This case concerns the ellipsoidal spherical slip surface that is partly replaced with a straight plane representing a weak seam, shown as Case 2 in Figure 8. This example, from Zhang[13], was also reevaluated by a number of authors, whose solutions are summarized in Table 2. Again, the special case of associative flow rule, $\phi = \psi$, has already been investigated by Chen et al.[1] giving F=1.767.

In the calculations with non-associative stress-strain relationships, the dilation angles of the slope material ψ changes from 0° to 20°, while the weak seam is always kept to be associative, i.e., ψ=ϕ =10°. Figure 10 shows an isometric view of the failure mass with inclined interfaces related to the critical mode.

Table 2 Comparison of the results from various authors for Zhang's example, Case 2

Zhang[13]	Hungr et al.[18]	Lam and Fredlund[14]	Huang and Tsai[15]	Chen et al.[1]	Chen et al.[17]
1.553	1.620	1.603	1.658	1.767	1.640

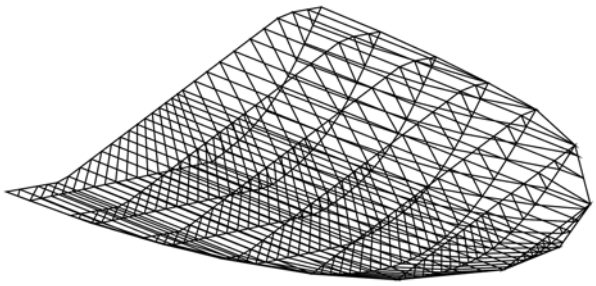

Figure 10 Case 2 of Zhang's Example 1, an isometric view of the failure mass with inclined interfaces.

Table 3 gives the factors of safety associated with different dilation angles from which one may find that F changes from 1.666 to 1.767, in a good agreement with the results of previous studies.

Table 3 Factors of safety associated with different dilation angles of ψ, Case 2 of Zhang's Example 1

ψ(°)	0	5	10	15	20
ψ_e(°)	0	2.97	5.88	8.76	11.64
F	1.666	1.687	1.713	1.739	1.767

4.2 The Xiangjiaba hydropower project

This project is located in the city of Yibin at which the rivers of Jingsha Jiang and Ming Jiang merge, creating the main course of the Yangtze River. Xiangjiaba is the last hydropower station among the Jingsha Jiang Cascade Development Plan. The total installed capacity of this currently built project is 6400 MW. Figure 11 shows the plan view of the scheme. The right part of the dam, of which the stability concern is investigated here, is composed of a surface power station and a flood discharge stilling basin. The foundation geology of this 159 m high concrete gravity dam consists of sandstone and mudstone with the Limeiwan Sincline passing through the dam axis, making the foundation highly inter-bedded and fractured. A typical cross section is shown in Figure 12. The potential slip surface consisting of the down-dipping bedding planes and adversely dipping joints or faults, as schematically shown in Figure 12, has been a critical concern of this project.

The stability analysis for concrete dam along potential weak seams in the foundation can be regarded as a

bearing capacity problem. In this computational sketch, the dam is regarded as a stack of concrete blocks that have no internal shear resistance against sliding but provide weight to the base of the slice, thus contributing to the mobilization of friction forces. The shear strength parameters on the interfaces between two contiguous concrete blocks are thus set to be zeros. Neglecting internal shear resistance among the dam body means a conservative approach in assessing the dam stability status. However, the shear resistance on the 'rock to rock' interfaces will be still considered.

1) The 2-dimensional analysis.

As mentioned previously, the failure mode under investigation consists of a down-dipping bedding plane representing $T_3^{2\text{-}3}$, designated by AB in Figure 12, and an adversely dipping fault-joint combination, designated by BC in Figure 12. The geotechnical parameters are listed in Table 4. Figure 13 shows the results of the 2-dimensional analyses for 11 sections of the stilling basin designated by S1 to S11. The weighted average 3D factor of safety is 3.036. As a common practice in concrete gravity dam design, a factor of safety exceeding 3.0 is required. It can be found that sections S1, S3, S4, and S9 fail to satisfy this criterion (Table 5).

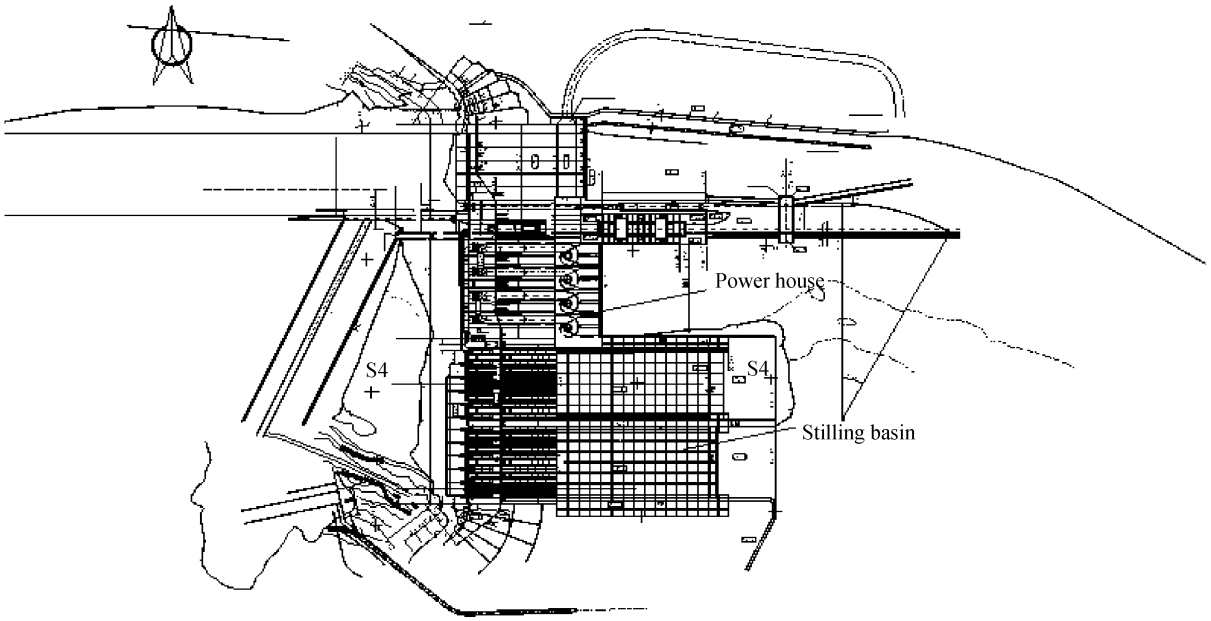

Figure 11 A plan view of the Xiangjiaba scheme.

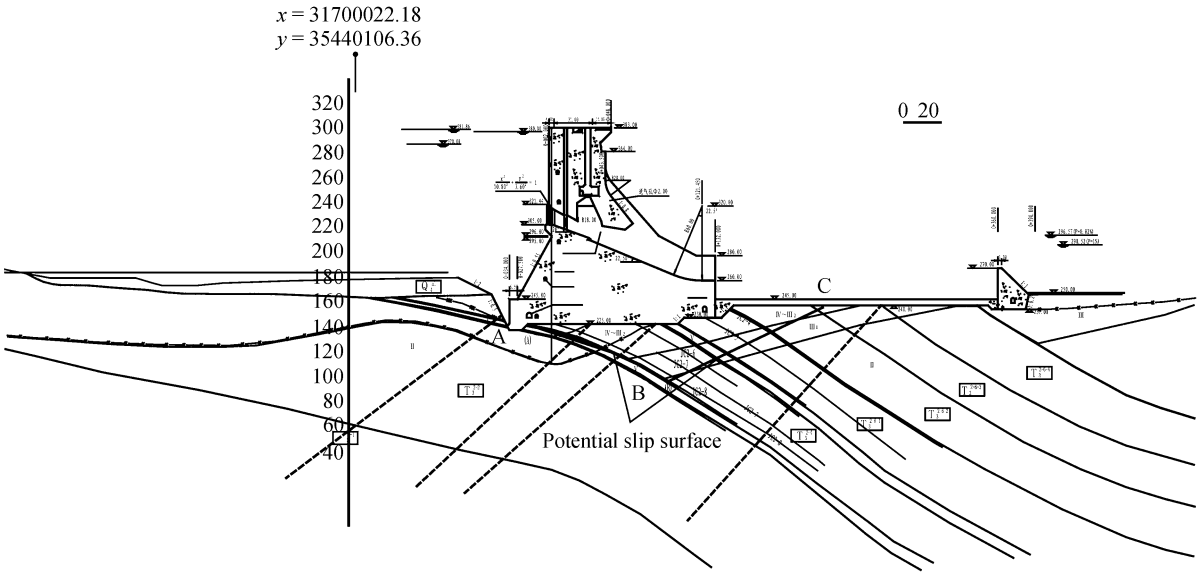

Figure 12 S4, a typical section of the concrete dam.

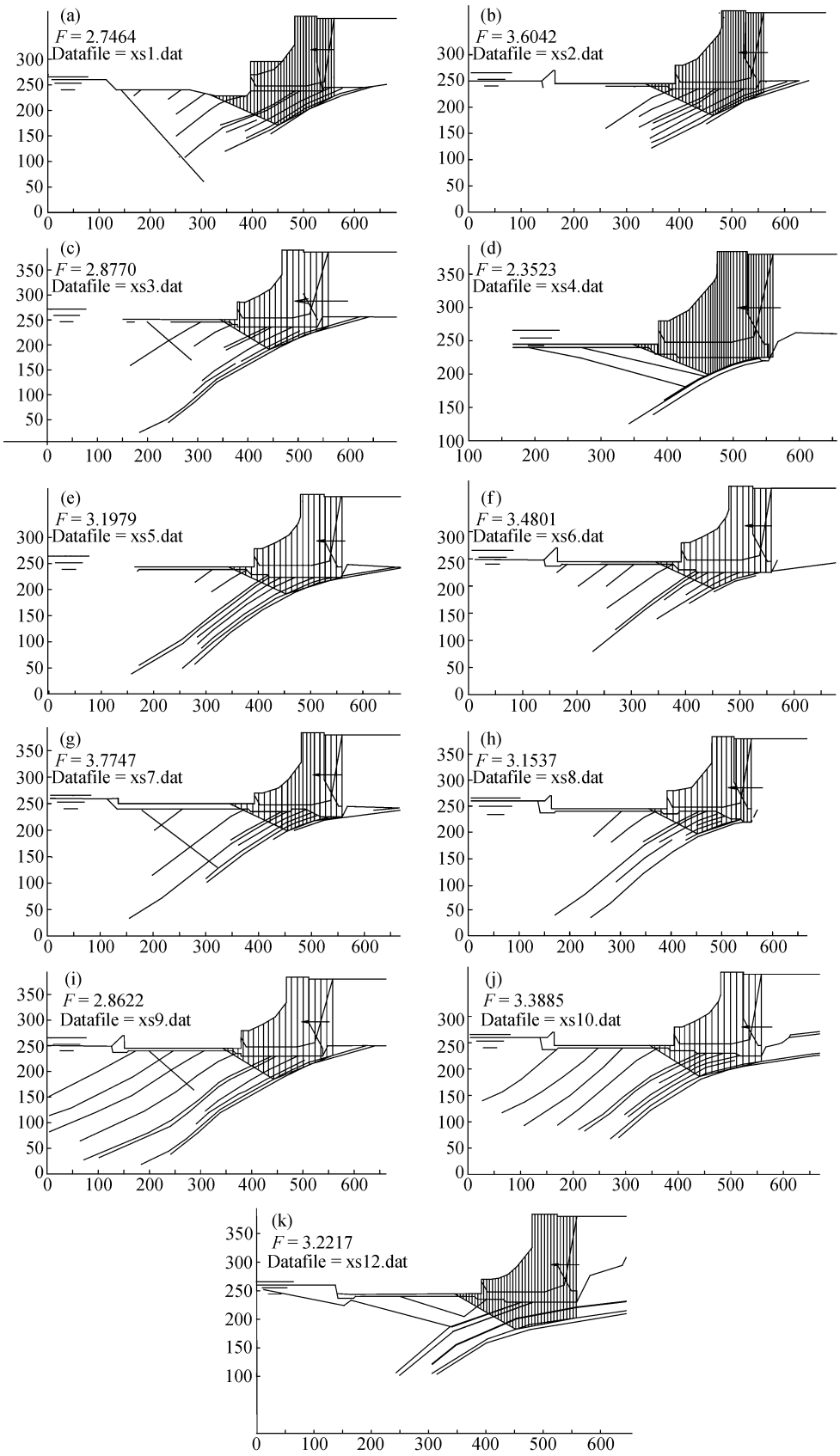

Figure 13 2D analyses for the stilling basin sections. (a) Cross section S1; (b) cross section S2; (c) cross section S3; (d) cross section S4; (e) cross section S5; (f) cross section S6; (g) cross section S7; (h) cross section S8; (i) cross section S9; (j) cross section S10; (k) cross section S11.

Table 4 Geotechnical property parameters

	Unit weight (kN/m^3)	Cohesion (kPa)	Friction angle (°)	Note
Concrete dam	24	2000	53	
Jointed rock mass II	26	1400	50.2	Used for part of BC in Figure 12
Jointed rock mass III1	26	1000	44.7	Used for part of BC in Figure 12
Jointed rock mass III2	26	800	40.8	Used for part of BC in Figure 12
Interface between rocks	26	300	15	
T_3^{2-3}	23	100	19.3	Used for part of AB in Figure 12

Table 5 Factors of safety of 2D analyses associated with cross sections S1 to S11

	S1	S2	S3	S4	S5	S6	S7	S8	S9	S10	S11
F	2.746	3.602	2.877	2.352	3.198	3.480	3.775	3.154	2.862	3.389	3.222

2) The 3-dimensional analysis.

It can be found in Figure 14 that the location of the down-dipping slip surface that daylights at the ground surface differs from section to section since the strike of the syncline that forms T_3^{2-3} is not completely parallel to the dam axis. At cross section 1, T_3^{2-3} daylights just at the dam heel (refer to Point A in Figure 12), while at S11 it is deeply imbedded in the foundation. Investigations of the 3D effect raised by the spatial variability of T_3^{2-3} is obviously of interest for better understanding to the actual stability status of the dam.

Calculations using the associative flow rule, i.e., $\phi=\psi$, fail to converge due to the large value of ϕ of the adversely dipping fault-joint combination (Part BC in Figure 12). As a compromise, c and ϕ are all set zero on the row-to-row and column-to-column interfaces. The factor of safety so obtained is 3.080. This approach is equivalent to the 3D simplified Janbu's method and is normally regarded as too conservative.

The 3D analysis using the non-associative stress-strain relationships described in this paper has been carried out. This allows the value of dilation angles of Part BC to be taken at a low value, making the calculations for plastic velocities converge.

In the calculations, the weak seam (Part AB) and the interface still adopt the associative flow rule, i.e., their dilations angles are 19° and 15°, respectively. Only Part BC of the slip surface employs dilation angles ψ varying from 0° to 30°. The shear strength parameters of the interfaces of rock masses have been assigned to be c=300 kPa and ϕ=15° as indicated in Table 4. Table 6 shows factors of safety at different ψ values. The 3-dimensional stability analysis with consideration of internal shear resistance between interfaces and reasonably large value of friction angles on the slip surface has been made possible. The associated factors of safety have been increased from an order of 3.0, associated with weighted average and simplified Janbu's method, to an order of 4.0 that represents the impact of considering the 3D effect due to the spatial variability of the slip surface.

Table 6 Factors of safety at different ψ values

ψ	0	10°	20°	30°	>30°
ψ_e	0	2.49	5.12	8.06	
Factor of safety	4.044	4.049	4.059	4.064	Non-convergent

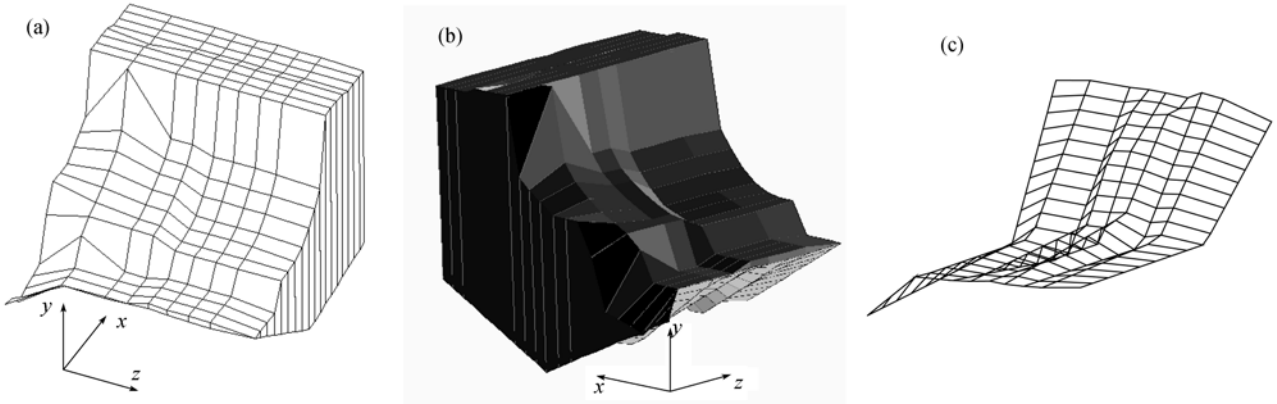

Figure 14 The isometric views of the 3D calculations. (a) 3D cross sections; (b) 3D image of the failure mass; (c) 3D image of the slip surface.

5 Summary and conclusion

(a) The research work presented here is the extension of the previous studies on 3-dimensional analytical methods for slopes. In terms of the failure surface, it extended a wedge to a generalized shape and in terms of the dilation angle, it allows an arbitrary angle compared to the friction angle required by the original approach that employs associative flow rule.

(b) The solution technique includes establishing the following two velocity fields.

1) The plastic velocity field $\boldsymbol{V}$ that follows a specified non-associative stress and strain relationship. A plane Λ that accommodates the shear force on the failure plane will be established once $\boldsymbol{V}$ is obtained.

2) The virtual velocity field $\boldsymbol{P}$ on plane Λ. $\boldsymbol{P}$ inclines at a friction angle to the failure plane. Applying work and energy balance equation for the whole system gives the factor of safety.

(c) Test examples have shown that this new method is applicable and the corresponding analytical results are consistent with those of previous studies. Use of the new method to Xiangjaiba dam shows that the new approach has got rid of convergence problems that have occasionally hampered the calculations in its practical applications where large friction angles of some materials are unavoidable.

1 Chen Z Y, Yin J H, Wang Y J. The three-dimensional slope stability analysis: Recent advances and a forward look. In: Han J, Yin J-H, White DJ, and Lin GM editors. Advances in Earth Structures: Research to Practice (ASCE Geotechnical Special Publication No.151). Shanghai: ASCE, 2006. 1－42

2 Donald I, Chen Z. Slope stability analysis by an upper-bound plasticity method. Can Geotech J, 1997, 4(11): 853－862

3 Sokolovski V V. Statics of Soil Media. Translated by Jones D H, Scholfield A N. London: Butterworth, 1960

4 Michalowski R L. Three-dimensional analysis of locally loaded slopes. Geotechnique, 1980, 39: 27－38

5 Farzaneh O, Askari F. Three-dimensional analysis of nonhomogeneous slopes. J Geotech Geoenviron Eng, 2003, 129(2): 137－145

6 Chen Z, Wang X G, Haberfield C, et al. A three-imensional lope stability analysis method using the upper-bound theorem. Part I: Theory and Methods. Int J Rock Mech Min Sci, 2001, 38: 369－378

7 Chen Z, Wang J, Wang Y, et al. A three-dimensional slope stability analysis method using the upper-bound theorem. Part II: Numerical approaches, applications and extensions. Int J Rock Mech Min Sci, 2001, 8: 379－397

8 Chen Z Y. A generalized solution for tetrahedral rock wedge stability analysis. Int J Rock Mech Min Sci, 2004, 41: 613－628

9 Chen W F. Limit Analysis and Soil Plasticity. New York: Elsevier Scientific Publishing Company, 1975

10 Pan J Z. Stability Analyses of Structures and Landslides (in Chinese). Beijing: Water Resources and Hydropower Press, 1978

11 Chen Z Y, Wang X G, Wang Y J, et al. Three-dimensional limit analysis of arch dam abutment stability (in Chinese). J Hydraul Eng, 2001, (8): 1－6

12 Chen Z Y, Wang X G, Xing Y C, et al. Theoretical study and physical modeling on 'Principle of Maximum' in slope stability analysis (in Chinese). Chinese J Geotech Eng, 2005, 27(5): 495－499

13 Zhang X. Three-dimensional stability analysis of concave slopes in plan view. ASCE J Geotech Eng, 1988, 114: 658－671

14 Lam L, Fredlund D G A. General limit equilibrium model for three-dimensional slope stability analysis. Can Geotech J, 1993, 30: 905－919

15 Huang C C, Tsai C C. New method for 3D and asymmetric slope stability analysis. ASCE J Geotech Environ Eng, 2000, 126(10): 917－927

16 Chen R H, Chameau J L. Three-dimensional limit equilibrium analysis of slopes. Geotechnique, 1982, 33: 31－40

17 Chen Z, Mi H, Zhang F, Wang X G. A simplified method for 3D slope stability analysis. Can Geotech J, 2003, 40: 675－683

18 Hungr O, Salgado F M, Byrne P M. Evaluation of a three-dimensional method of slope stability analysis. Can Geotech J, 1989, 26: 679－686